Supplementary Materials for

Mapping Local Charge Recombination Heterogeneity by Multidimensional Nanospectroscopic Imaging

Wei Bao, M. Melli, N. Caselli, F. Riboli, D. S. Wiersma, M. Staffaroni, H. Choo, D. F. Ogletree, S. Aloni, J. Bokor, S. Cabrini,* F. Intonti, M. B. Salmeron, E. Yablonovitch, P. J. Schuck,* A. Weber-Bargioni*

*To whom correspondence should be addressed. E-mail: afweber-bargioni@lbl.gov (A.W.-B.); scabrini@lbl.gov (S.C.); pjschuck@lbl.gov (P.J.S.)

Published 7 December 2012, *Science* **338**, 1317 (2012)
DOI: 10.1126/science.1227977

This PDF file includes:

Materials and Methods

Numerical Simulation

Simulations of the electromagnetic wave distribution were performed using the commercial finite element method (FEM) based software COMSOL Multiphysics 4.2. Frequency dependent relative permittivity of gold $\varepsilon_2(\omega) = \varepsilon_r - i\varepsilon_i$ used for simulation was taken from Palik's handbook (*32*) and the refractive index of the SiO_2 layer was set as n=1.5.

Structural parameters of campanile probe in the simulations, unless defined otherwise, were as follows: d=50 nm, θ =30^o , Wo=20 nm, Li=200 nm, Wi=200 nm, Do=10 nm, Di=200 nm. It was placed in the center of a volume with a refractive index n=1. This box was surrounded by 6 layers (100 nm) of Perfect Matched Layers (PML) on five sides to avoid unphysical reflections from the sides. A plane wave with electric field component Ey=1 V/m instead of HE_{11} mode was sent from the base of the campanile structure, since the linearly polarized transverse mode is the dominant fundamental HE_{11} mode in NSOM optical fibers (*33*). All PMLs were placed far away from the metal structures to avoid spurious effects coming from a potential interaction between the evanescent waves and the PML. This was assured by a convergence study. Ten layers of mesh were used in the terminating nano-gap to guarantee accuracy and mesh independent results. The field enhancement is strongest at the Au film edge but the ultra-sharp edges in the simulation makes the convergence of the simulation in the imaging plane (~1 nm away from the apex) difficult with a low density of meshing (D_0=10 nm >>1 nm). To circumvent the lack of memory issue, the maximum electric field enhancement near the apex in the xz-symmetric plane is recorded (the mirror plane in between the two tapered metal plates) to make a conservative estimation of the maximum electric field enhancement in the imaging plane. This will slightly underestimate the maximum value in the imaging plane, but enables realistic, convergent and mesh-independent results 3 layers away from the computation singularity. All the enhancement results were extracted from the maximum value of the electric field E_{max} in xz-symmetry plane of the campanile and normalized with the incident electric field Ey. Note that the ultimate resolution of our

probes is primarily limited by gap size and/or the sharpness of the metal-dielectric interface, not the skin depth of the metal. This is because of the discontinuity in the normal component of the E-field that exists at the metal-dielectric interface, leading to a large, sharp jump in E-field strength at this interface.

Campanile probe fabrication

3M single mode optical fibers for 633 nm (2.5 μm core diameter) were wet-etched with concentrated HF to shape a smooth cone with a tip radius of 100 nm. Using Focused Ion Beam (FIB) milling (Zeiss Crossbeam 1540), the campanile geometry was carved into the etched glass fiber tip. Using shadow evaporation, 50 nm thick Au with a 2nm adhesion layer was evaporated on two opposing sides of the campanile structure. Typically the resolution of the angle resolved evaporation was not sufficient to create a well-defined gap between the two triangular plates at the tip apex. Hence, a gap was cut at the tip apex, using FIB, resulting in a gap typically 40-50 nm wide and 30 nm long, as shown in Figure 2B. The fabrication resolution can be increased by optimizing the milling process, alternative fabrication procedures or by using a Helium FIB. For the measurements presented here 7 fibers were produced and all of them worked.

Sample preparation

The indium phosphide nanowires were prepared by Chemical Vapor Deposition (MOCVD) using Trimethylindium TMI and tertbutylphosphine TBP as In and P sources respectively. The nanowires were grown on a Si(111) substrate with a 2 nm thick gold film acting as catalyst for the nanowire formation. The substrate was annealed in-situ at 600 deg C prior to the introduction of the TMI and TBP resulting in a distribution of 10-20 nm in diameter gold clusters on the surface. The nanowires were grown at 415^0 C for 10 minutes with an In molar fraction of ~2 10^{-6}, V/III ratio of 40, and under a total flow of 8 l/min of H_2. The as grown substrates consist of 1- 5 μm long and 30-100 nm thick nanowires. TEM analysis shows that the wires have a zinc blend structure and grow in the [111] direction with clean and often atomically flat cleaved ends. The nanowires single crystals are covered with a very thin (~ 1nm) thick amorphous layer most from oxidation in air. Their shapes are mostly cylindrical with a minority that exhibits some

faceting resulting in hexagonal cross-sections. The as-grown nanowires are then dry transferred to 100nm thick SiO_2 on p++ Si(100) patterned with alignment marks to allow us to interrogate the same nanowire with multiple techniques.

Optical measurement

The optical measurements were done with two different instruments. The Near Field Measurements were done on an Omicron a Scanning Near Field Optical Microscope [TwinSNOM, Omicron] using a shear force head in illumination/collection geometry. The campanile fibers were glued on the piezo-bimorph with a resonance frequency of ~ 60 kHz. Using the shear force microscope, the campanile tips were scanned over the InP NW sample, using the phase as feedback. A 633nm laser passed through a laser line filter, 50/50 beam splitter and was coupled with 100μW into the back of the campanile glass fiber. The signal obtained back through the campanile tip and glass-fiber was directed through the 50/50 beam splitter and a 695 nm long pass filter, and on to a calibrated cooled spectrometer, where it was dispersed and finally detected by a cooled InGaAs array. We control the polarization of the light in the SNOM experiment by using a non-polarization maintaining fiber and a polarization compensator acting on the fiber. Each photon, collected by the probe, changes its polarization state during the propagation along the fiber. This unknown polarization change is, however, identical for all the collected photons and therefore is fully compensated. The polarization compensation is obtained using a system based on the Babinet–Soleil compensator that permit to apply a controlled pressure and rotation to the fiber. At each pixel, a full optical spectrum was recorded. The data analysis of the 3D spectral matrix was analyzed by a custom written matlab program. All data presented here are raw data.

The confocal measurements were done with an NT-MDT spectra microscope on the same InP NWs investigated using near-field microscopy. A 633 nm HeNe laser was used with a line filter with control over polarization. A 100x, 0.7 NA objective was used to excite the sample and collect the signal. The signal passed through a dichroic filter, focused through a 50 μm pinhole onto a calibrated, Peltier-cooled spectrometer. Again, hyperspectral maps were recorded and the analysis done via the NT-MDT analysis software.

Supplementary Text

Comparing the campanile geometry to state of the art plasmonic structures employed for imaging

The effect of the campanile geometry on the enhancement in the xy-symmetry plane was investigated by varying first the width W_i at the base of the campanile structure, and later the distance D_i that separates the metallic plates at the base and third the gap between the plates at the tip apex D_0. Figure S1 illustrates the normalized electric field enhancement $M=E_{max}/Ey$ while varying the W_i, D_i and D_0 parameters.

The width dependence is shown in Figure S1 D from which one can deduce a square root dependence between the enhancement M and the width: The width is defined as a multiple C of 100nm via $Wi = C \times Wc$, with Wc=100 nm. The enhancement gradually follows a square root dependence of the multiplier C via $M= \sqrt{C} \times Ec$, with $Ec \approx 26$ being constant. In contrast, varying the width does not influence the resonance frequency of the campanile structure.

The influence of the separation of the two metallic plates D_i is illustrated in Figure S1 E, and Figure S1 F displays the enhancement versus the gap distance D_0. A 10nm gap will give already a near field enhancement of roughly 20, where 10 nm gap size corresponds to the best achievable resolution using state of the art fabrication tools such as He+ Focus Ion Beam lithography (FIB). The plot illustrates also that the enhancement can be strongly increased by reducing the gap size well below 10nm.

Based on these results a field enhancement can be predicted for a campanile geometry: Assuming a campanile tip structure at the end of a glass fiber with a rectangular base of 3~4 μm, tapered down in 3 dimensions to a $20\ nm \times 10$ nm gap at the apex results in a relative electric field enhancement in the imaging plane on a dielectric material of ~125 ($\sqrt{3\mu m / 100nm} \times 25$). Based on the above scaling trends in the smaller scale simulation, all the relative enhancement numbers in the main text will be multiplied by a geometric factor 5 ($\sqrt{3\mu m / 100nm} \approx 5.5$) as the second normalization step to predict what happened in larger size.

In order to show the conversion between photonic mode light and plasmonic

mode light as in Figure 1E, we also simulated a Wi=Di=1500 nm and film =300 nm campanile structure and plot with the color saturation at the electric field value of 2.5 V/m (i.e. – much of the field is saturated). This allows us to show the distribution of the less-localized fields in/near the structure.

We next simulated a 30 nm thick gold bowtie antennae, shown in Figure 1F, composed of two equilateral triangles with the length of sides L=75 nm. The triangles are rounded with R=5 nm radius at the vertex and separated 2 nm with each other. Normalized enhancement is defined as the ratio of the maximum electric field on the xy-symmetry plane and the incident light Ey=1V/m.

As a comparison, 15 μm long conical adiabatically tapered (CAT) gold probe with a 20 nm radius of curvature and a cone semi angle of 15 degrees was also simulated by directly defining a magnetic current at the base of the cone. The normalized enhancement is defined by the ratio of maximum electric field 1 nm away from the probe and 3rd loop of the standing SPP wave away from the magnetic current source. This also means the coupling efficiency from the far-field illumination into the SPP in this simulation is 100%, which is an over-estimated value.

Coupling efficiencies between far-field and near-field

Scattering losses during propagation are minimized since the plasmons travel along the smooth inner dielectric/metal interfaces. More recently, calculations have suggested that the 3D linear tapering approach could focus 830 nm light into a 2-by-5 nm^2 area with $\leq$ 3 dB loss.

Resolution vs. throughput dilemma in conventional NSOM probes

A conventional near field probe is a metal-coated etched glass fiber, with a sub-diffraction limited aperture at the apex. The size of the aperture determines the spatial resolution. These probes are background-free and broadband, but for apertures smaller then ~100 nm, there is very little light leaking out the aperture leading to very low signal-to-noise ratio. Exciting and collecting signal through the same aperture, especially for collecting a full spectrum at each pixel, is nearly impossible for conventional aperture-based probes with a diameter below 100nm. This has to do with cut-off of the

propagating far-field modes in the conventional aperture based probe. We exemplify this here with a simulation.

Typically, a 30-100 nm thick metallic cladding (often Al) is employed to confine the light inside the fiber and funnel it to the nanoscale aperture. However, this metal boundary implies boundary conditions on the EM wave traveling inside the fiber leading to a mode cut-off, including the SPP mode, before reaching the aperture (compare Fig. SOM 2). This visualizes the resolution vs. throughput dilemma in conventional NSOM probes for the past two decades. Fig. SOM 2 illustrates a normalized field distribution of a conventional NSOM probe. The radius at the base of the cone representing the tapered NSOM fiber is 166 nm with a semi-angle of the cone structure of 20^{o}. The cone is covered with a 50 nm thick Au film aside from the tip apex, forming a 10 nm radius aperture. In the simulation this NSOM probe is excited with both linearly polarized light and radially polarized light ($|E|=1$ V/m). Figure SOM 2 illustrates the propagation retention of the electromagnetic wave before it reaches the aperture for both linearly (Fig. SOM 2A) and radially polarized light (Fig. SOM 2B) due to the tapered induced mode cut off resulting in an exponentially intensity decrease of the electric field at the tip apex.

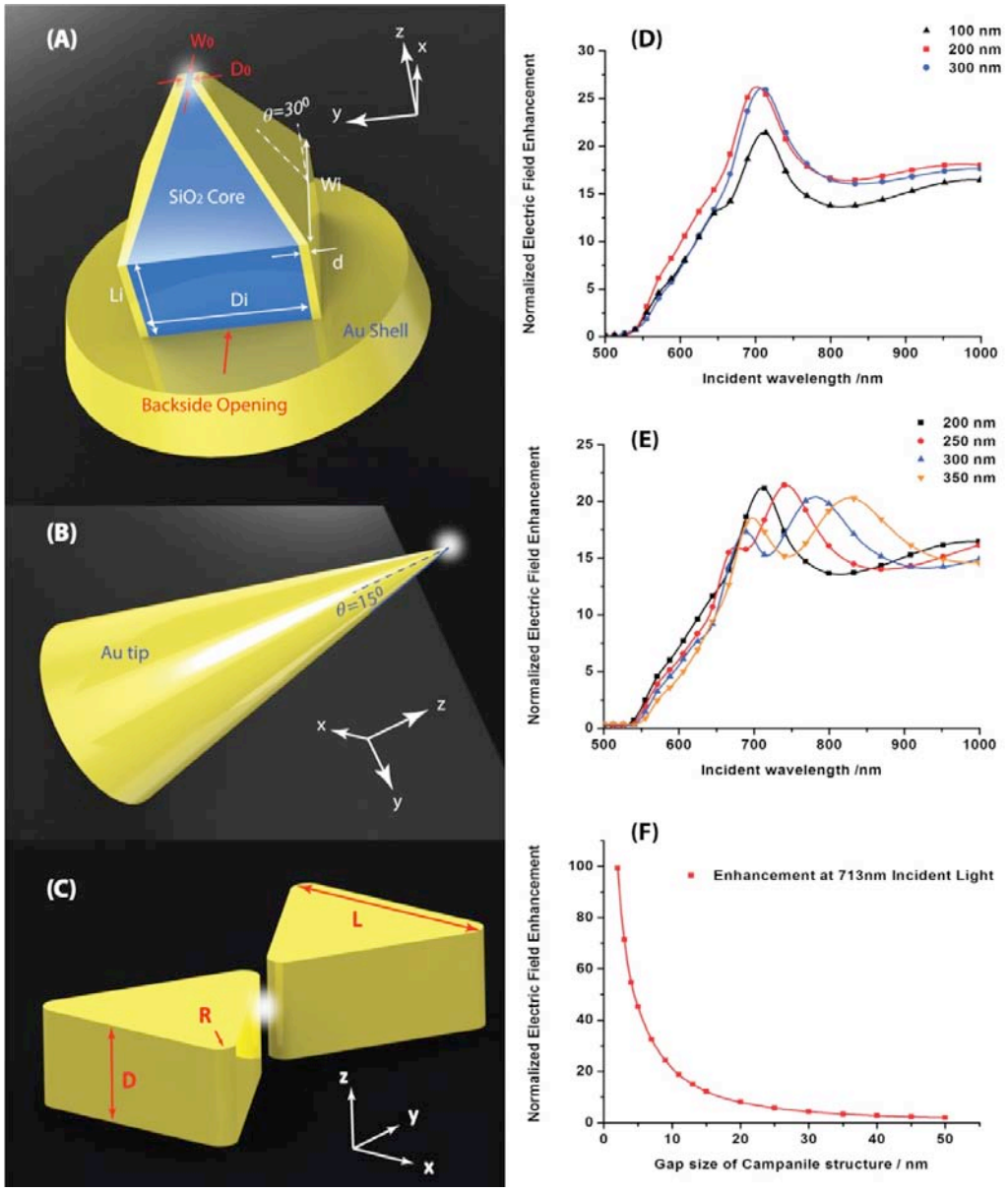

Fig. S1

Illustration of the geometries used in the simulations and normalization calculations of the electric field enhancement. 3D Schematic drawing of (A) campanile probe, (B) Cylindrical probe, and (C) Bowtie antennae. The graphs on the right side show the variation of normalized maximum electric field amplitude $M/\sqrt{C}$ at the end of the campanile probe for different structural parameter: (D) W_i (E) D_i (F) D_o. Default structural parameters for campanile probes in these simulations were as follows: d=50 nm, $\theta=30^o$, W_o=20 nm, L_i=200 nm, W_i=100 nm, D_o=10 nm, D_i=200 nm.

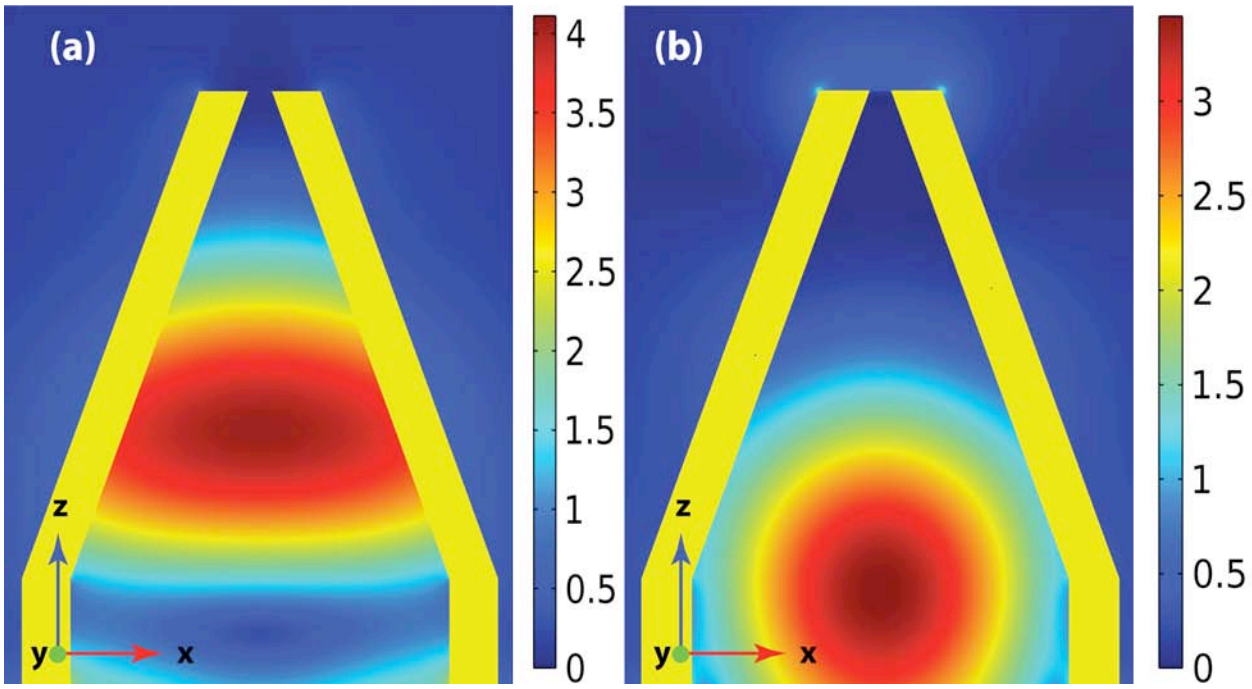

Fig. S2
The cross section through a traditional cone like NSOM probe and the steady-state electric field normalized to the amplitude of the incident field for (A) linearly polarized E_x wave and (B) radially polarized E_r wave. For this simulation, λ_o = 632 nm was used.

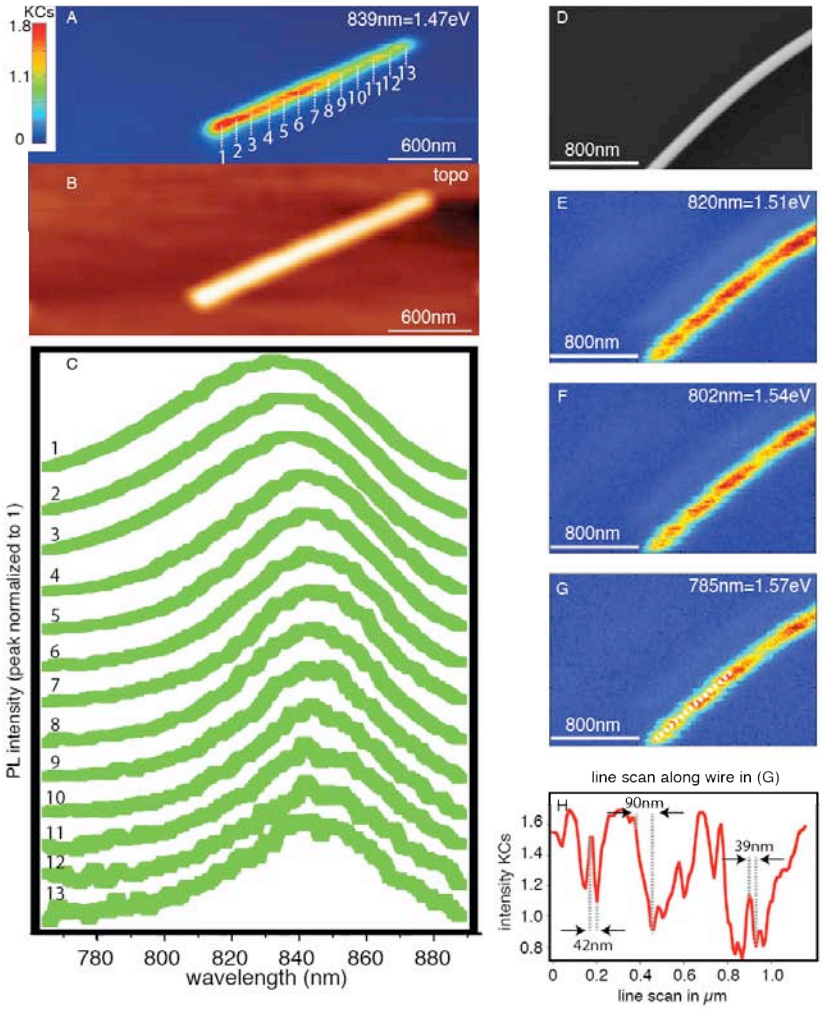

Fig. S3

Spectral and intensity variation of the local PL signal along individual InP NWs. A) Shows a strong increase in the band edge PL intensity with the parallel recorded topography image (B). A waterfall of spectra (C) taken along the wire and the intensity normalized to 1 shows a broadening of the spectra from 40 nm to 70 nm along the wire, where the broadest spectra corresponds to the highest intensity in the PL map. D) A slightly curved InP NWs shows PL intensity heterogeneity along the wire (E-G) at different energies, mostly pronounced for energies above the band edge. The PL intensity varies over 200% along the wire and can change locally within 40nm –the resolution limit of the campanile tips employed for this work.

References

1. R. Hillenbrand, T. Taubner, F. Keilmann, Phonon-enhanced light matter interaction at the nanometre scale. *Nature* **418**, 159 (2002). doi:10.1038/nature00899 Medline

2. L. Novotny, B. Hecht, *Principles of Nano-Optics* (Cambridge Univ. Press, Cambridge, 2006).

3. S. Kawata, Y. Inouye, P. Verma, Plasmonics for near-field nano-imaging and superlensing. *Nat. Photonics* **3**, 388 (2009). doi:10.1038/nphoton.2009.111

4. D. Zhang *et al*., Nanoscale spectroscopic imaging of organic semiconductor films by plasmon-polariton coupling. *Phys. Rev. Lett.* **104**, 056601 (2010). doi:10.1103/PhysRevLett.104.056601 Medline

5. J. Stadler, T. Schmid, R. Zenobi, Developments in and practical guidelines for tip-enhanced Raman spectroscopy. *Nanoscale* **4**, 1856 (2012). doi:10.1039/c1nr11143d Medline

6. Y. Wang, W. Srituravanich, C. Sun, X. Zhang, Plasmonic nearfield scanning probe with high transmission. *Nano Lett.* **8**, 3041 (2008). doi:10.1021/nl8023824 Medline

7. J. N. Farahani, D. W. Pohl, H. J. Eisler, B. Hecht, Single quantum dot coupled to a scanning optical antenna: A tunable superemitter. *Phys. Rev. Lett.* **95**, 017402 (2005). doi:10.1103/PhysRevLett.95.017402 Medline

8. A. Weber-Bargioni *et al*., Hyperspectral nanoscale imaging on dielectric substrates with coaxial optical antenna scan probes. *Nano Lett.* **11**, 1201 (2011). doi:10.1021/nl104163m Medline

9. P. D. Yang *et al*., Controlled growth of ZnO nanowires and their optical properties. *Adv. Funct. Mater.* **12**, 323 (2002). doi:10.1002/1616-3028(20020517)12:5<323::AID-ADFM323>3.0.CO;2-G

10. D. Roy, J. Wang, C. Williams, Novel methodology for estimating the enhancement factor for tip-enhanced Raman spectroscopy. *J. Appl. Phys.* **105**, 013530 (2009). doi:10.1063/1.3056155

11. C. C. Neacsu *et al*., Near-field localization in plasmonic superfocusing: A nanoemitter on a tip. *Nano Lett.* **10**, 592 (2010). doi:10.1021/nl903574a Medline

12. F. De Angelis *et al*., Nanoscale chemical mapping using three-dimensional adiabatic compression of surface plasmon polaritons. *Nat. Nanotechnol.* **5**, 67 (2010). doi:10.1038/nnano.2009.348 Medline

13. M. Staffaroni, J. Conway, S. Vedantam, J. Tang, E. Yablonovitch, *Photonics Nanostructures Fundam. Appl.* **10**, 166 (2012).

14. M. I. Stockman, Nanofocusing of optical energy in tapered plasmonic waveguides. *Phys. Rev. Lett.* **93**, 137404 (2004). doi:10.1103/PhysRevLett.93.137404 Medline

15. P. Ginzburg, D. Arbel, M. Orenstein, Gap plasmon polariton structure for very efficient microscale-to-nanoscale interfacing. *Opt. Lett.* **31**, 3288 (2006). doi:10.1364/OL.31.003288 Medline

16. S. Vedantam *et al*., A plasmonic dimple lens for nanoscale focusing of light. *Nano Lett.* **9**, 3447 (2009). doi:10.1021/nl9016368 Medline

17. E. Peytavit, J. F. Lampin, T. Akalin, L. Desplanque, Integrated terahertz TEM horn antenna. *Electron. Lett.* **43**, 73 (2007). doi:10.1049/el:20073679

18. J. F. Wang, M. S. Gudiksen, X. F. Duan, Y. Cui, C. M. Lieber, Highly polarized photoluminescence and photodetection from single indium phosphide nanowires. *Science* **293**, 1455 (2001). doi:10.1126/science.1062340 Medline

19. J. M. Bao *et al*., Optical properties of rotationally twinned InP nanowire heterostructures. *Nano Lett.* **8**, 836 (2008). doi:10.1021/nl072921e Medline

20. K. Cho *et al*., *Appl. Phys. Lett.* **98**, 203101 (2011).

21. A. Franceschetti, A. Zunger, Optical transitions in charged CdSe quantum dots. *Phys. Rev. B* **62**, R16287 (2000). doi:10.1103/PhysRevB.62.R16287

22. S. A. Fischer, C. M. Isborn, O. V. Prezhdo, Excited states and optical absorption of small semiconducting clusters: Dopants, defects and charging. *Chemical Science* **2**, 400 (2011). doi:10.1039/c0sc00626b

23. L. K. van Vugt, S. J. Veen, E. P. A. M. Bakkers, A. L. Roest, D. Vanmaekelbergh, Increase of the photoluminescence intensity of InP nanowires by photoassisted surface passivation. *J. Am. Chem. Soc.* **127**, 12357 (2005). doi:10.1021/ja051860o Medline

24. N. Yamamoto, S. Bhunia, Y. Watanabe, *Appl. Phys. Lett.* **88**, 153106 (2006). Medline

25. E. Shafran, B. D. Mangum, J. M. Gerton, Using the near-field coupling of a sharp tip to tune fluorescence-emission fluctuations during quantum-dot blinking. *Phys. Rev. Lett.* **107**, 037403 (2011). doi:10.1103/PhysRevLett.107.037403 Medline

26. J. J. Greffet, Applied physics. Nanoantennas for light emission. *Science* **308**, 1561 (2005). doi:10.1126/science.1113355 Medline

27. S. Kühn, U. Håkanson, L. Rogobete, V. Sandoghdar, Enhancement of single-molecule fluorescence using a gold nanoparticle as an optical nanoantenna. *Phys. Rev. Lett.* **97**, 017402 (2006). doi:10.1103/PhysRevLett.97.017402 Medline

28. H. J. Maas *et al*., Imaging of photonic nanopatterns by scanning near-field optical microscopy. *J. Opt. Soc. Am. B* **19**, 1295 (2002). doi:10.1364/JOSAB.19.001295

29. M. L. M. Balistreri, H. Gersen, J. P. Korterik, L. Kuipers, N. F. van Hulst, Tracking femtosecond laser pulses in space and time. *Science* **294**, 1080 (2001). doi:10.1126/science.1065163 Medline

30. P. Vasa, C. Ropers, R. Pomraenke, C. Lienau, Ultra-fast nano-optics. *Laser Photon. Rev.* **3**, 483 (2009). doi:10.1002/lpor.200810064

31. M. Seo *et al*., Active terahertz nanoantennas based on VO2 phase transition. *Nano Lett.* **10**, 2064 (2010). doi:10.1021/nl1002153 Medline

32. E. D. Palik, G. Ghosh, Knovel (firm), *Handbook of Optical Constants of Solids* (Academic Press, San Diego, CA, 1998).

33. K. Okamoto, *Fundamentals of Optical Waveguides. Optics and Photonics* (Academic Press, San Diego, CA, 2000).